Optimization of a Fluidic Vortex Generator's Control in a Transonic Channel Flow

Quentin Chanzy, Eric Garnier, Reynald Bur

Optimization of a Fluidic Vortex Generator's Control in a Transonic Channel Flow

Quentin Chanzy,* Eric Garnier,† and Reynald Bur‡
ONERA–Paris Saclay University, F-92190 Meudon, France

https://doi.org/10.2514/1.J058873

Flow control of separation caused by transonic shock-wave/boundary-layer interaction (SWBLI) is investigated. The control of the unsteadiness associated with SWBLI is not an objective of this paper. A SWBLI in a transonic channel is considered, and Reynolds-averaged Navier–Stokes simulations are carried out to compute the flow in the test section. The massive separation due to the interaction is controlled by fluidic vortex generators (VGs). Ten VGs are positioned in the center of the test section according to analyses based on physical considerations and literature results. A first kriging-based optimization is used to determine the most appropriate pitch and skew angles of the VGs. The optimum configuration found is then considered, and a second kriging algorithm is used to enhance the control of the corner flow by adding two VGs. The longitudinal and lateral locations and the pitch and skew angles of the two lateral VGs are optimized. The objective of these optimizations is to minimize the total pressure losses through the shock-wave/boundary-layer interaction. A configuration improving the objective function by 61% is found with slightly upstream-blowing jets. To understand this original finding, a comparison of the vorticity patterns generated by downstream- and upstream-blowing jets is therefore carried out.

Nomenclature

c_μ	=	momentum coefficient
DC50	=	criterion of homogeneity and efficiency
Hi	=	boundary-layer incompressible shape parameter
Ma	=	Mach number
n	=	number of calculated points
P	=	static pressure, Pa
$\bar{P}_i$	=	dimensionless stagnation pressure
p	=	parameter of the ψ function
q	=	dynamic pressure
Re_θ	=	Reynolds number based on momentum thickness
S	=	surface, m^2
T	=	temperature, K
U	=	velocity, $m \cdot s^{-1}$
X	=	longitudinal coordinate, m
Y	=	vertical coordinate, m
$\bar{Y}$	=	vertical distance from the lower wall, m
y^+	=	dimensionless wall distance
Z	=	lateral coordinate, m
α	=	pitch angle, deg
β	=	skew angle, deg
δ	=	boundary-layer physical thickness, mm
δ_j	=	boundary-layer physical thickness at the position of the jets, mm
δ_1	=	boundary-layer displacement thickness, mm
Θ	=	parameter of the ψ function
θ	=	boundary-layer momentum thickness, mm
ρ	=	density, kg/m^{-3}
$\bar{\rho}U$	=	dimensionless longitudinal momentum
ψ	=	basis function of the kriging model
ω	=	longitudinal vorticity, s^{-1}
$\bar{\omega}$	=	dimensionless longitudinal vorticity

Subscripts

B	=	barycenter of $\|\omega\|$
jets	=	jets
k	=	dimension of the model
st	=	stagnation conditions
zone	=	one of the 50 zones of the DC50

Superscript

i	=	referring to the ith calculated point

I. Introduction

CONCEIVING air intakes remains a challenge during the design process of a supersonic or hypersonic aircraft. The difficulty lies in the fact that shock waves inherent to these devices may interact strongly with the turbulent boundary layers. The well-known shock-wave/boundary-layer interaction (SWBLI) phenomenon often provokes flow separation, wich leads to losses, distortions, and unsteadiness. This kind of interaction has been widely studied (see Refs. [1–4] among others), and the instationarities have been associated with the separation bubble dynamic. To prevent these inconveniencies, several control techniques have been studied: bleeding, blowing, adaptive geometries like two-dimensional (2-D) and three-dimensional (3-D) bumps, diverters, vortex generators (VGs) (see Refs. [5–8] for examples of reviews of the proven control methods), and more recently dielectric barrier discharge (see Ref. [9]) and plasma devices (see Ref. [10]). Fluidic control has proven to be a very versatile control mean that, for example, has been successfully employed to manage the transition process in compressible flows (see Refs. [11,12]). These methods require a close consideration of the complete problem. They should improve the efficiency of an air intake: their added mass and relative energy efficiency having to be taken into account. The scope of the physic field of flow control is detailed, including its fallacies and limits in Ref. [13]. In the present study, the authors choose to investigate the air jet VGs from a full 3-D point of view. This control method seems promising because it displays the same potential as the mechanical VGs to reduce the separated zone extent (see Refs. [14–17]). Furthermore, it has the advantages of being energy efficient, generating less intense shock waves than the mechanical VGs, thus improving the air intake efficiency; and it can easily be turned off when not necessary.

The interaction between a perpendicular jet and a transverse flow has been widely studied and is well documented (see Refs. [18–21]).

Received 22 July 2019; revision received 4 June 2020; accepted for publication 5 June 2020; published online 6 October 2020.

*Ph.D. Student, Aerodynamic Aeroelastic Acoustic Department, 8 rue des Vertugadins; quentin.chanzy@onera.fr.

†Research Scientist, Aerodynamic Aeroelastic Acoustic Department, 8 rue des Vertugadins; eric.garnier@onera.fr.

‡Research Scientist, Aerodynamic Aeroelastic Acoustic Department, 8 rue des Vertugadins; reynald.bur@onera.fr.

It produces a counter-rotating pair of vortices that can be used to enhance the mixing of the boundary layer with the external flow. Several experimental studies have been devoted to this type of control, using normal or pitched and skewed jets: most of them with jets blowing in the same direction as the mainstream [22–24].

The diversity of vorticity structures produced by pitched and skewed jets has been investigated and described in Refs. [25,26], with these studies being restricted to jets blowing in the downstream direction.

Continuous advances in computational power allow us to consider optimization processes, taking into account the numerous parameters involved in this type of control. The present study considers an optimization process, focusing on the skew and pitch angles of air jet VGs and the control of the global interaction including separation and corner flow effects.

This numerical study is realized on the Délery bump configuration of the S8Ch wind tunnel of the ONERA Meudon Center, which is detailed in Refs. [17,28,29] and presented in Fig. 1. The shape of the bump was designed to induce a strong interaction between the boundary layer and a shock at a nominal Mach number of 1.4, which generates an extended separated zone. As shown in Fig. 2 [27], the interaction exhibits a λ shock pattern. The latter can be decomposed in two parts; the first one is composed of weak oblique shock wave S1 and near-normal "trailing" shock S2, and the second one is composed of normal shock S3. These two parts merge at triple point I. This structure separates the flow in four states. The upcoming flow (point 1) is modified, respectively, into points 2 and 3 by shock waves S1 and S3. And, finally, the state at point 2 is changed into the state at point 4 by the rear leg of the λ shock. The states at points 3 and 4 are compatible (i.e., different velocities but same static pressure level) on both sides of the slip line.

In what follows, the numerical model is presented in Sec. II and the optimization process is detailed in Sec. III. In a third step, in Sec. IV, it is applied to the boundary-layer separation for 10 fluidic VGs. After this, a second stage of optimization specifically dedicated to the control of the corner flow separation is carried out in Sec. V. Finally, in Sec. VI, the vorticity patterns induced by upstream- and downstream-blowing VGs are investigated in order to interpret the results of the optimizations.

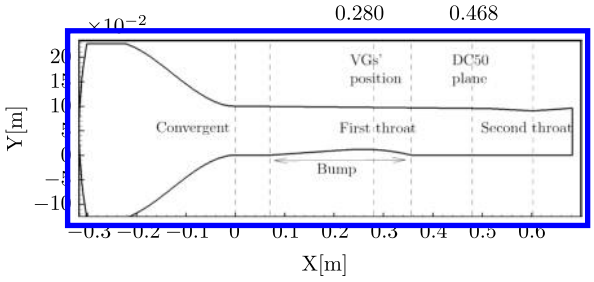

Fig. 1 S8Ch wind tunnel's geometry.

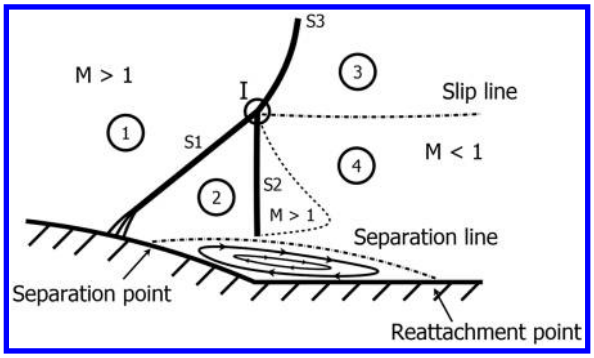

Fig. 2 Shock-wave/boundary-layer interaction (from Ref. [27]). The λ shock-wave structure is broken down into three different shocks: S3 is the normal shock wave; and S1 and S2 are, respectively, the front and rear legs of the λ shocks.

II. Numerical Model

A. Overset Meshes

First of all, in order to avoid meshing several times the whole wind tunnel for each air VG's configuration, overset meshes are employed. The whole preprocess is handled using the ONERA software Cassiopée [30].

The meshes are shown in Fig. 3: the principle being to have a very refined mesh (in blue in Fig. 3) close to the VGs position in order to fully capture the flow issuing from the jets and their interaction with the incoming boundary layer. The sizes of the cells of this mesh match those used to mesh the jets. The numbers of grid points of these meshes are given in Table 1. Close to the walls, the cell wall-normal distances are lower than 2 μm, which results in a dimensionless wall distance y^+ smaller than one almost everywhere; the grid point distribution in the wall-normal direction then follows a geometric law of ratio 1.1. The boundary-layer thicknesses are described using about 50 points, which allow capturing at the location of the experimental measurements, a boundary-layer thickness of $\delta = 3.3$ mm, a displacement thickness of $\delta_1 = 0.42$ mm, and an incompressible shape parameter of $Hi = \delta_1/\theta = 1.33$. These values are close to the ones measured using laser Doppler velocimetry in the wind tunnel in Ref. [17]: physical thickness $\delta = 3.9$ mm, displacement thickness $\delta_1 = 0.46$ mm, and incompressible shape parameter $Hi = 1.6$.

B. Boundary Conditions and Initial States

The stagnation conditions of the flow are close to ambient pressure and temperature: $P_{st} = 0.96 \cdot 10^5 \pm 300$ Pa and $T_{st} = 300 \pm 10$ K. The associated unit Reynolds number is around 14×10^6 m^{-1}, which leads to a value of $Re_\theta = 3500$ for the incoming flow.

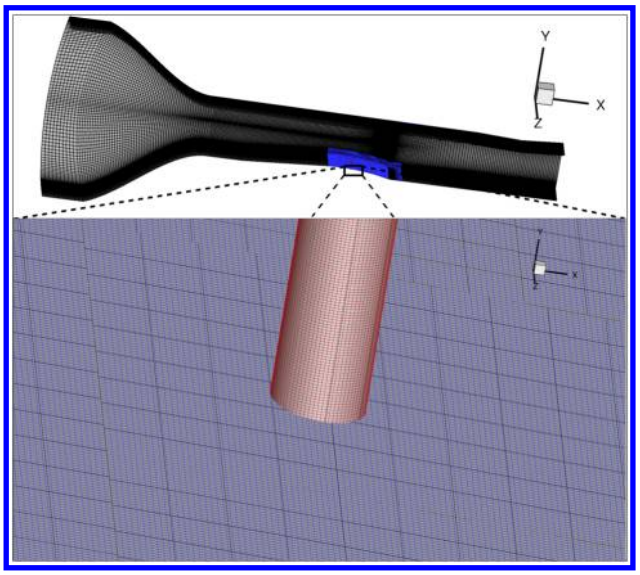

Fig. 3 Overset meshes of the wind tunnel with fluidic VGs: fine mesh (blue), jets' meshes (red), and coarser mesh (black).

Table 1 Mesh characteristics

	Number of points			
	Total	X direction	Y direction	Z direction
Unitary jet	252,681	57	57	143
Mesh in the jets vicinity	60,839,100	1073	60	945
Whole wind-tunnel mesh	4,922,640	344	159	90

To accelerate the convergence of the calculations, three initial states were used, corresponding to the same stagnation conditions of $P_{st} = 0.96 \times 10^5$ Pa and $T_{st} = 300$ K at various Mach numbers. For the first initial state, a Mach number of Ma $= 0.01$ is imposed on the convergent part of the channel; for the second state, Ma $= 0.6$ is imposed in the central part of the test section, including the first throat associated with the bump. In the last one, a state with Ma $= 1.3$ is used to start the second throat, which controls the mass flow rate.

At the wind-tunnel entrance, a subsonic condition is imposed using the stagnation pressure and the stagnation enthalpy corresponding to the first state. At the end of the diffuser, a supersonic outflow condition is imposed. As the mesh represents only a half of the wind tunnel, a symmetry condition is imposed on the median plane. Everywhere else, a no-slip condition is imposed.

When the jets are added, the coarser mesh is blanked by a finer mesh using a Cassiopee function [30]. The process called the chimera method is illustrated in Fig. 4: the fine mesh is represented by the yellow zone, with the nonblanked cells of the coarser mesh being visible. The interpolation cells are located at the intersection of both regions. At least two cells of each mesh are kept inside of the overset mesh in order to perform a proper interpolation. Other examples of the use of this method can be found in Ref. [31]. Furthermore, the lower wall of the fine mesh is set to a doubly defined condition, meaning that the wall is considered as a viscous wall. Yet, the cells of the wall of the fine mesh crossed by the cells of a jet are considered as overlap boundaries.

C. Solver

The structured Reynolds-averaged Navier–Stokes (RANS) computations are executed with the ONERA in-house software elsA [32], which uses a cell-centered finite volume discretization on structured and overset grids. The spatial and time integrations are, respectively, carried out using an upwind second-order Roe scheme with a Harten entropic correction and a backward-Euler scheme with implicit lower/upper symmetric successive over-relaxation.

Turbulence is modeled using the one-equation Spalart–Allmaras model supplemented with the quadratic constitutive relation (QCR) correction [33]. This correction complements the Boussinesq relation with anisotropic terms, which improve the model accuracy in the corner flow separation zone.

The calculations are processed on a cluster: more precisely, on 256 cores distributed on 10 processors. It takes an equivalent of 3800 CPU hours to achieve 30,000 iterations and a proper convergence of the residuals.

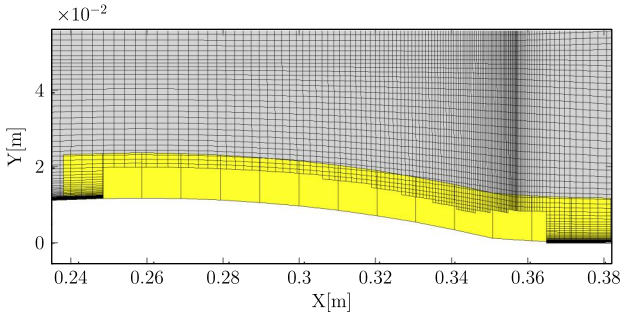

Fig. 4 Illustration of the blanking process.

D. Reference Case

The uncontrolled reference case is calculated as a validation purpose. The computed flow in the wind-tunnel symmetry plane is compared to 2-D particle image velocimetry (PIV) results obtained by Sartor et al. [28] in Fig. 5. The streamwise velocity fields compare well; the extent of the separated zone is well predicted, with its height being slightly overestimated. The green cells in the red and blue areas in Fig. 5a are the cells of the fine mesh outside of the interpolation zone, and thus are not to be associated with an error in the computation.

To validate the QCR correction, a colored surface flow visualization was experimentally performed and compared to the skin-friction lines of the RANS calculation for the corner flow separation on the sidewall in Fig. 6. The location and size of the corner flow separation are qualitatively well predicted by the model, which confirms the

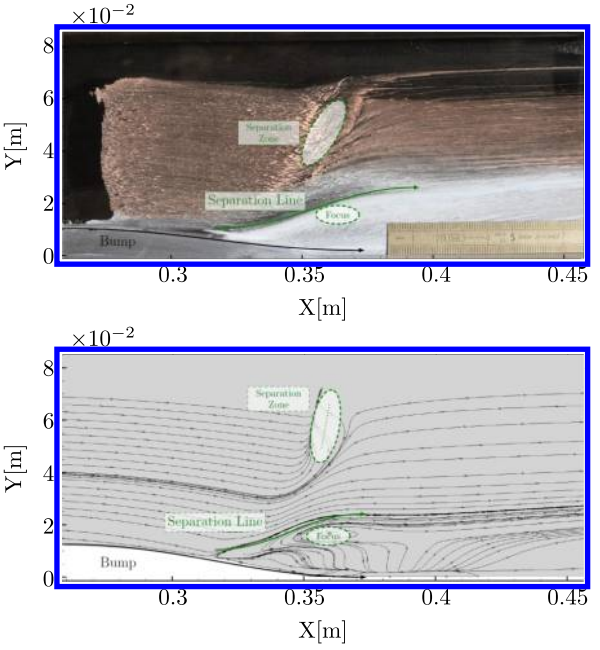

Fig. 6 Comparison between an experimental colored oil visualization (top) and the friction lines of the RANS calculation (bottom) for the corner flow separation on the lateral wall.

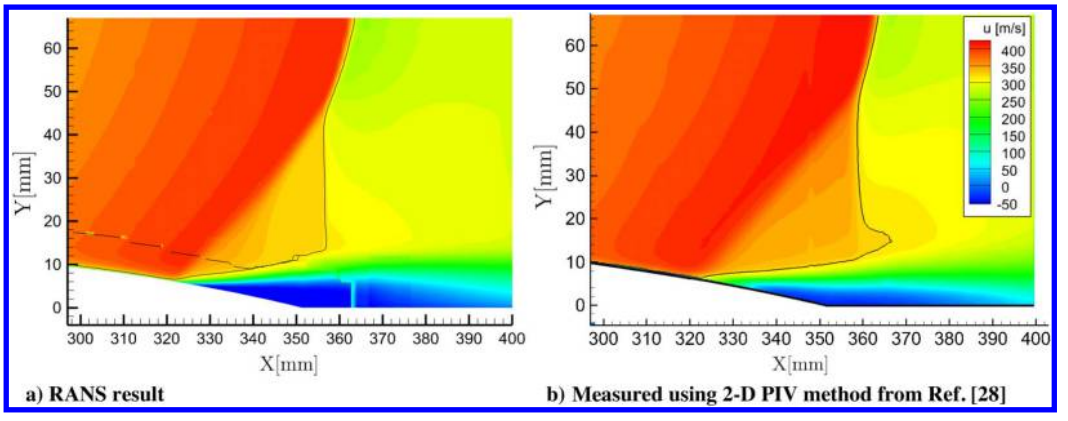

Fig. 5 Longitudinal velocity field at the symmetry plane of the wind tunnel; the black line represents the sonic line.

interest of the QCR correction for a fine enough mesh in a confined configuration, contrary to previous results obtained for a wing/body separated flow [34].

III. Optimization Approach: An Algorithm Based on Kriging Metamodel

To choose several control parameters, an optimization method is built up: the idea being to minimize an objective function presented in Sec. IV.B with respect to parameters defined in Secs. IV.A and V.A. Since the phenomena linked to the interactions between a jet and a crossflow and between a vortex and a shock wave are really nonlinear, an algorithm based on the kriging model is chosen. This method has been widely used in various optimization processes, such as porous media behaviors [35], aerodynamic design [36], and fluid–structure interaction [37]. It has the advantage of not assuming the smoothness of the function. Furthermore, since the objective function can be very flat with only very localized maxima, this method of search should be faster than a conventional Newton method. Another technique would have consisted of running an adjoint-state method to compute the gradient. Nevertheless, the size of the mesh is still a huge obstacle to its application; and this method is not yet compatible with overset meshes in the elsA software.

The different sequences of the optimization process are described in Algorithm A1.

To initiate the optimization, a sampling plan is defined. The Latin hypercube method implemented in Ref. [38] is used to find the best Latin hypercube sampling, following the criterion function in Ref. [39].

After evaluating the sampling plan, the kriging method is used to construct a first model. This method is explained in Refs. [38,40,41]. The main idea when building a model is to use a basis of functions, which allows computing of the model at each point of the exploration space.

In kriging, the basis functions $\psi^i(x)$ used to construct the model are defined following Eq. (1), with each ith one linked to an ith calculated point of the n points already measured:

$$\psi^i(x) = \exp\left(-\sum_{k=1}^{n} \Theta_k |x_k^i - x_k|^{p_k}\right) \tag{1}$$

with x_k^i and x_k as the coordinates in the kth dimensions of, respectively, x^i and x, the ith calculated point, and the evaluation point. The Θ_k and p_k are variable parameters.

These functions are close to Gaussians with parameters Θ_k and p_k, which allow balancing of the influence of each sample point in every dimension in order to find the best model. These functions take advantage of the fact that the validity of the model is more certain close to a calculated point, as well as the fact that the function can change more or less rapidly near each calculated point. In this case, only the Θ_k parameters are optimized by using a genetic algorithm, whereas the p_k parameters are kept equal to two.

To improve the model, points are added using the expected improvement function [38], which permits us to look for improvement close to an optimum of the model and to take into account model uncertainty in the less known area of the parameter space. This allows switching from a phase of improvement of the solution to a phase of exploration.

To get a less noisy model, regression kriging is used to compute the final results presented hereafter. The regression kriging presented in Ref. [38] is a variant of the kriging model where a constant term is added to the model in order to take into account the fact that there is some noise into the infill data, and thus to allow the model not to interpolate all the calculated points. This constant value is also optimized using the same genetic algorithm.

IV. First Optimization: The Separation Control

A. Optimization Parameters

Achievement of the control depends on a wide variety of parameters: the numbers of jets, their crosswise and streamwise locations, their injection pressure, and their pitch and skew angles. To keep the calculation time reasonable, only two parameters are optimized in a first approach: the pitch and skew angles. The others parameters are chosen thanks to first trials and literature results on the mechanical micro-VGs. The basic configuration is defined as follows: 10 VGs are positioned in the spanwise direction of the channel, separated by 2.1 δ (with a bigger gap in the center of the channel due to the presence of a pressure sensor) and 12 δ in front of the SWBLI, which was the best location determined in a previous study carried out with mechanical VGs on the same experimental device [17]. The locations of the jets, which can be seen on half of the wind tunnel in Fig. 7, correspond to an abscissa of $X = 0.280$ m. The injection total pressure is fixed to 2 bars. The jets diameters are set to 1 mm to ensure a small velocity ratio and a small momentum coefficient c_μ, as defined in Eq. (2), which are the main criteria of efficiency for such fluidic control devices. The velocity ratio comprises between 1.5 and 2 for the different studied configurations. The fluidic jets are quantified by using the momentum coefficient c_μ defined by [42]

$$c_\mu = \frac{\Sigma \rho_{\text{jet}} U_{\text{jet}}^2 S_{\text{jet}}}{0.5 \rho U^2 S} \tag{2}$$

in which ρ and U are the density and the velocity in the upstream part of the channel (assumed uniform), and S is the channel section.

It should be noticed that the real shape of the injection hole is an ellipse that varies with the pitch and skew angles.

Furthermore, the VGs are oriented with counter-rotating angles. Previous studies (Ref. [43] for instance) demonstrated that even if the

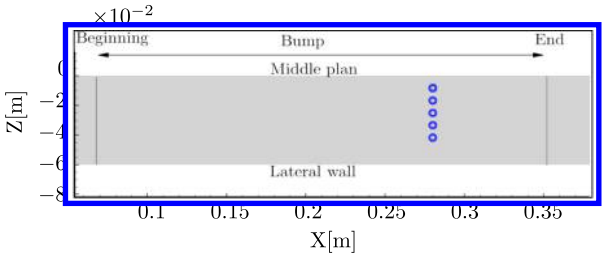

Fig. 7 Positions of the jets.

Algorithm A1: Kriging-based optimization

1: Sampling plan
  a) Generation of the initial sampling with a Latin hypercube method
2: Observations
  a) Evaluation of these designs with elsA; see Sec. II.
3: Construction of the surrogate
  a) Construction of a surrogate model using kriging method.
4: Search of the infill criterion
  a) Construction of the model of the expected improvement
  b) Search of the maximum of the expected improvement thanks to a particle swarm optimization algorithm.
5: Addition of a new design
  a) Evaluation with elsA of the new design at the maximum of the expected improvement function.
  b) Addition of the new design to the model and return back to step 3.

vortices generated by a counter-rotating pair of VGs are more likely to interact and to generate a zone in between with a velocity deficit, they sustain each other, and thus promote a better mixing elsewhere. Moreover, in a rectangular channel, corotating VGs cause a lateral velocity, which strongly affects corner flows.

The two angles of the jets are defined in Fig. 8 with respect to the local streamwise and crosswise tangents. Due to physical constraints (the unfeasibility of drilling a hole with a 1 mm diameter at very small angles), the pitch angle α is varied between 30 and 150 deg only. The skew angle β is varied between 0 and 180 deg. Combined with the pitch rotation, this variation allows consideration of all the physical configurations, including the upstream-blowing jets, which have benefited from less attention in the literature.

B. Objective Function: DC50 Criterion

The goal of this study is to reduce the separation zone; this should improve both the homogeneity and the total mechanical energy of the flow downstream of the SWBLI. To quantify the improvement of these quantities, a distorsion criterion DC50 based on an existing criterion used by aircraft manufacturers (the DC60 criterion [44,45]) has been defined. The DC50 criterion is calculated in a plane perpendicular to the flow direction located downstream of the separation zone at $X = 0.468$ m, as shown in Fig. 9a. This plane coincides with the location of a mobile pitot probe rake. The criterion defined in Eq. (3) consists of a comparison between the spatial mean stagnation pressure Pi in the considered plane and the worse (lowest) spatial mean stagnation pressure in the 50th part of the plane $\mathrm{Pi}_{\mathrm{zone}}$. This quantity is divided by the mean dynamic pressure q in the plane in order to give information both on the homogeneity of the flow and on the energy conservation. The 50 parts of the plane for the reference case (without control) are presented in Fig. 10a, where the losses of stagnation pressure due to the boundary layer and the corner flow separation are clearly visible. The DC50 of the reference case is equal to 0.88. The objective of the optimization is to minimize this value.

$$\mathrm{DC50} = \frac{\langle \mathrm{Pi} \rangle - \min(\langle \mathrm{Pi} \rangle_{\mathrm{zone}})}{\langle q \rangle} \tag{3}$$

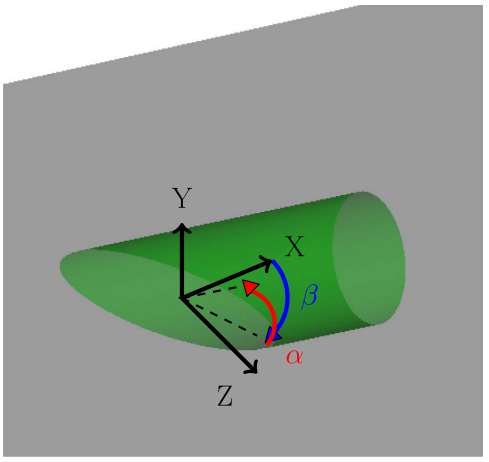

Fig. 8 Definitions of α and β, respectively, pitch and skew angles.

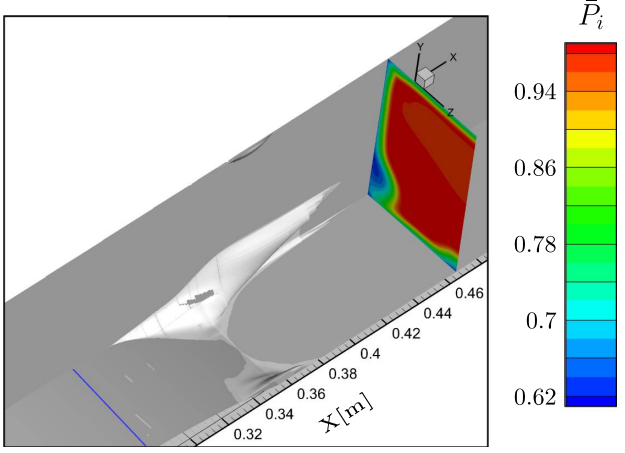

Fig. 9 Nondimensionalized stagnation pressure on the DC50 plane, and volume of the reverse flow (delimited by the white surface) for the reference case (the blue line represents the position of the VGs).

C. Results

The process of optimization is illustrated in Fig. 11, with the dots representing the calculated points. Their colors are associated with their rank in the optimization process; the seven first sampled points are white, and the dots are getting darker as the optimization progresses.

Six remarkable configurations are designated as points a to e. They correspond to vertical jets, aligned downstream-blowing jets, aligned upstream-blowing jets, a suboptimum case, the optimum case, and a

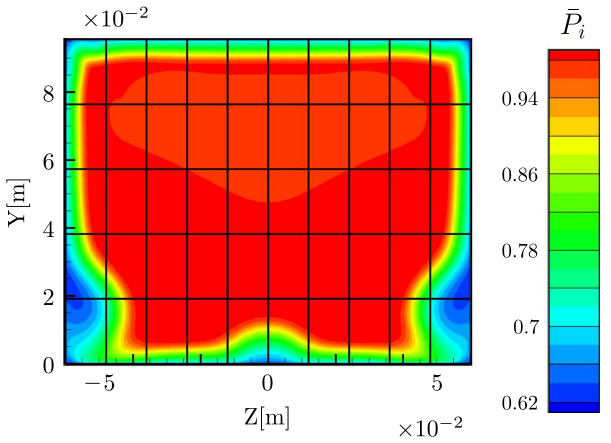

Fig. 10 Nondimensionalized stagnation pressure on the transverse plane of the reference case used for the DC50 calculation delimited into the 50 zones.

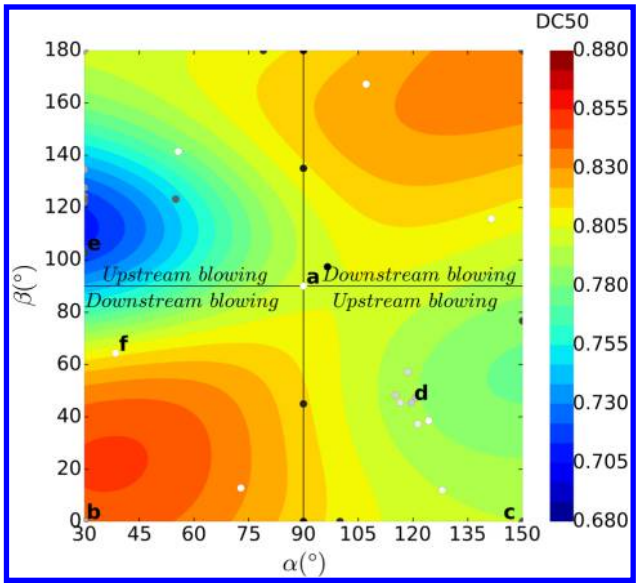

Fig. 11 Regression kriging model of DC50 function with respect to skew and pitch angles of 10 VGs. Dots represent calculated cases: the first sampled ones are white, and the other ones get darker with respect to their order of infill.

case close to the classical control configuration ($(\alpha, \beta) = (30, 60$ deg) [46–48]). Their physical geometries are shown in Fig. 12, and the diverse vorticity patterns they generate are presented in Fig. 13 (the vorticity is nondimensionalized using $U(X = 0) = 250$ m $\cdot$ s^{-1} and δ_j). These vorticity patterns are more deeply studied in Sec. VI.

As shown in Fig. 11 with the DC50 model, the algorithm first finds a zone of interest close to point d, where several points are added. Then, the algorithm starts a second exploration and manages to find another zone of interest close to point e. In a third step, after several enrichments, the algorithm starts a third exploration, during which it does not manage to find a new interesting zone of interest even after adding three new points. Then, the model is no longer modified, with the values of the newly calculated points being close to the ones predicted by the model, and thus the optimization is considered as converged.

To add more physical considerations in the model, independent of the optimization process, four points are added at no additional numerical cost since they correspond to the same configuration. Indeed, when the pitch angle is set to 90 deg, the skew angle no longer has real signification because the jets remain vertical with respect to the local streamwise and crosswise tangents.

The final model is presented in Fig. 11; it interpolates the points within a 3% error margin following the philosophy of regression kriging.

The upper and lower limits of the model corresponding to $\beta = 0$ deg and $\beta = 180$ deg are similar but with opposite direction, following the variation of α, which means that for $\beta = 0$ deg, the increase of α follows the same variation as the decrease of α for $\beta = 180$ deg. This is a fair result since for the jets without lateral deviation, when β is changed from 0 to 180 deg, the jets are directed in the opposite direction, with the α angle corresponding to its complementary angle to 180 deg. For example, the configuration of $\beta = 0$ deg and $\beta = 60$ deg is exactly the same as $\beta = 180$ deg and $\alpha = 120$ deg.

The model presents a "quasi-central symmetry," which is consistent with the fact that the intensity and location of the vortices generated by the jets symmetric with respect to the centers of the model are symmetric along the longitudinal plane. The difference of the DC50 level is due to the fact that the jets close to the center and the corner of the channel interact differently and that there is an even number of jets in this configuration. In Fig. 11, the two main zones of interest in blue and green are in the upstream-blowing jet zones, which differ from the previous studies where the preferential angles were $\alpha = 30$ deg and $\beta = 60$ deg [46–48].

The best controlled case found is for $\alpha = 30$ deg and $\beta = 102.8$ deg values of angles, the objective function being equal to 0.68 which represents already an improvement of 22% with respect to the baseline case. It generates the stagnation pressure distribution presented in Fig. 14 and the whole flow topology is visible in Fig. 15. This configuration is composed of upstream blowing jets with the lateral one pointing outward at the wall. The external jet manages to reduce the impact of the corner flow by inducing a reverse flow farther from the lateral wall compared to the baseline case presented in Fig. 9. The corner flow presents a completely different shape and seems to be more efficiently dissipated. Due to the fact that in this

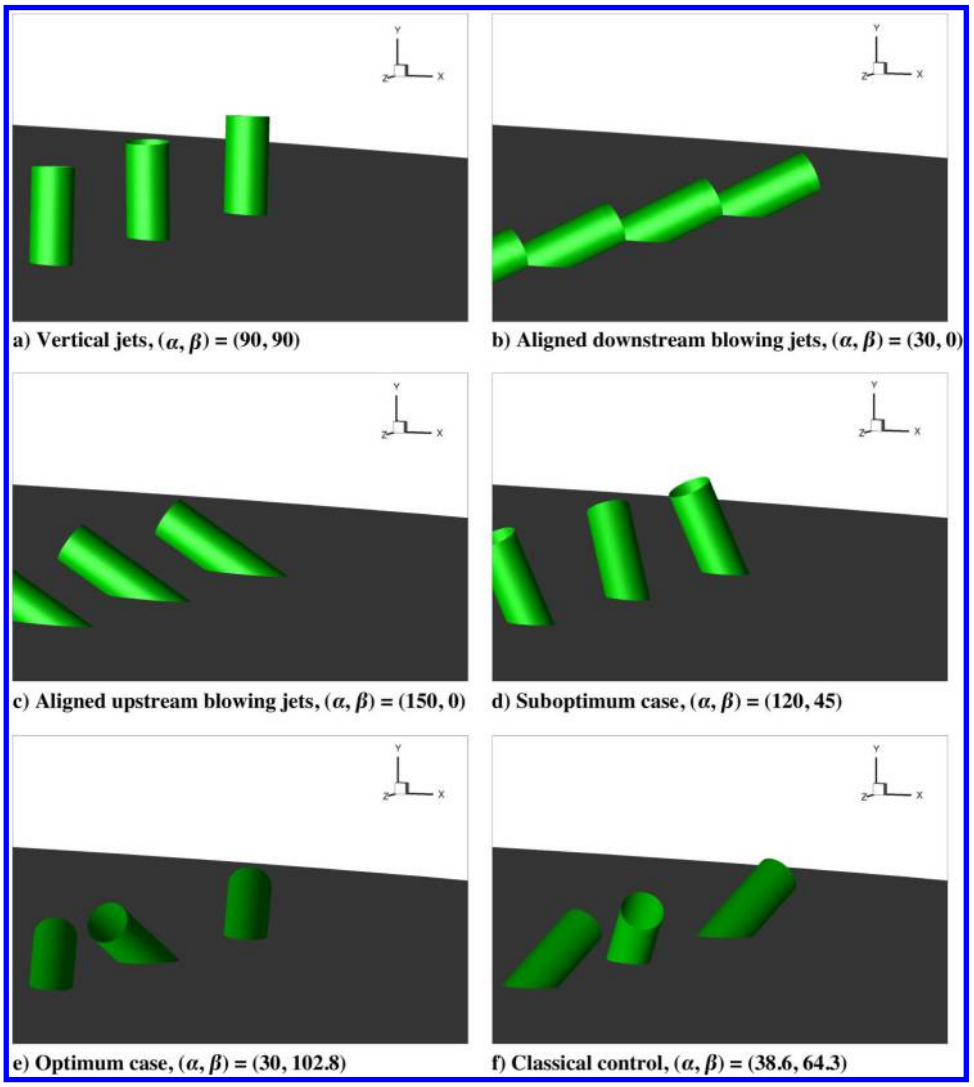

Fig. 12 Physical geometry of jet configurations studied more precisely; the letters correspond to the ones on the DC50 model in Fig. 11.

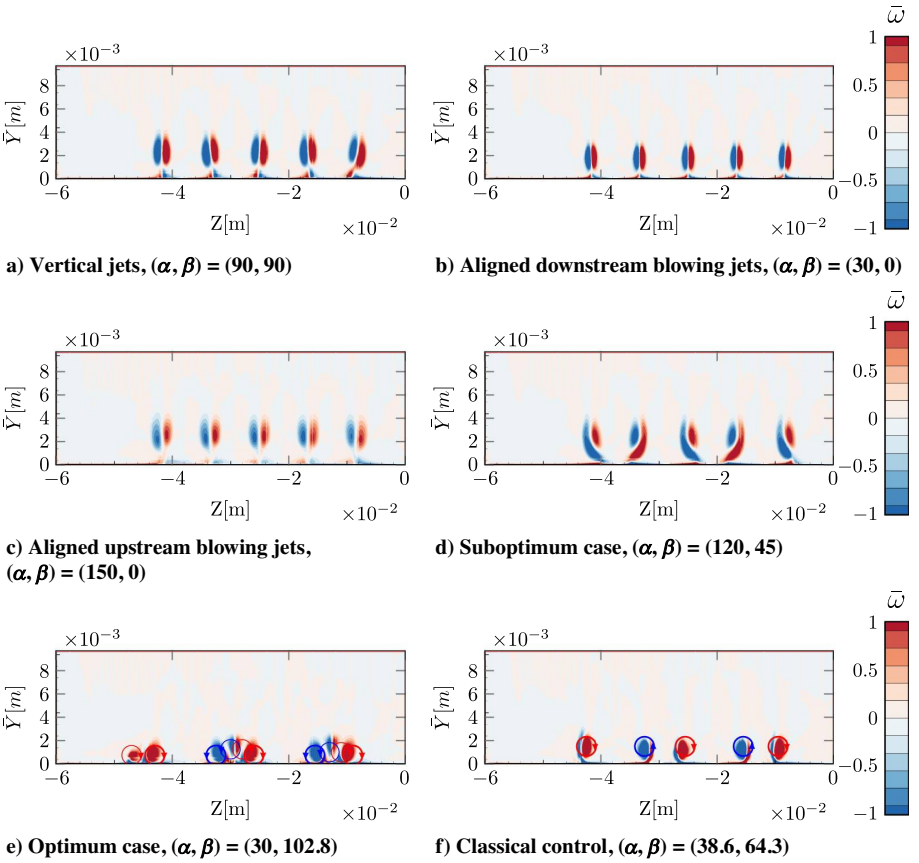

Fig. 13 Vortices produced by VG configuration on a transverse plane at $X = 0.290$ m; the letters correspond to the ones on the DC50 model in Fig. 11.

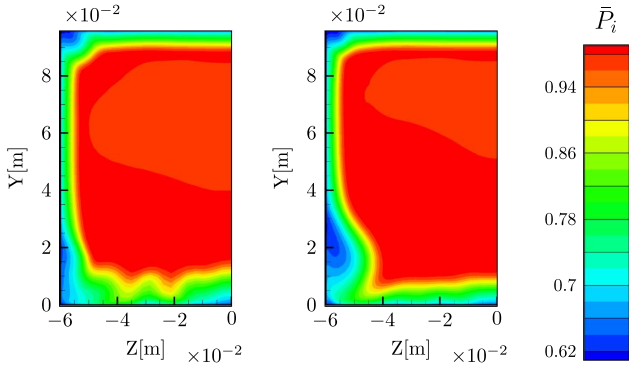

Fig. 14 Nondimensionalized stagnation pressure on the transverse DC50 plane of the best-controlled cases of the first optimization.

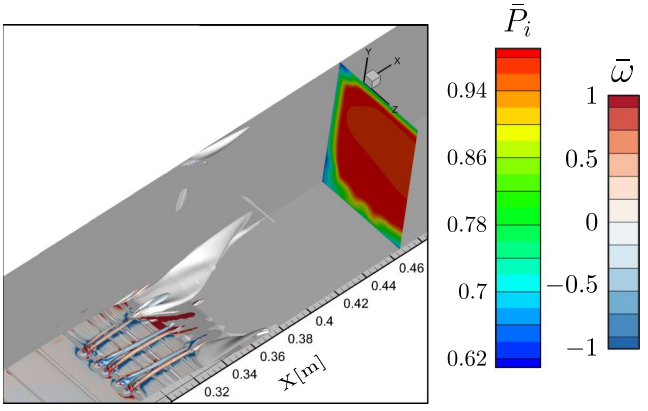

Fig. 15 Nondimensionalized stagnation pressure on DC50 plane, volume of reverse flow (delimited by white surface), and Q criterion equal to $3 \cdot 10^8$ isosurface colorized with longitudinal vorticity for optimum case.

configuration the two central jets are pointing outwards, the central separation is diminished but not completely removed. The reduction of corner flow separation however, impacts more the DC50 criterion.

The conclusion of this first optimization is that the algorithm managed to find an optimum that reduces the value of the objective function with a configuration made of slightly upstream-blowing jets. Nevertheless, this study emphasizes the fact that the most important contribution of the control is achieved by the outer jet, which controls the corner flow separation. This separation is responsible for the main variations of the DC50. The importance of the corner flow separation has already been pointed out in Refs. [49,50]. To further improve the control, a second optimization is considered with a specific jet controlling the corner flow. In order to avoid the growth of the reverse flow in the center of the channel while the corner separation diminishes, a central control is conserved. The case chosen for this control variant is the suboptimum case with $\alpha = 120$ deg and $\beta = 45$ deg, presented in Figs. 14b and 16a. It generates a DC50 of 0.78, which is an improvement of only 11% compared to the baseline case. However, it better controls the central separation and, since the outer jet is pointing inward, it will not interact with the outer jet added to control the corner flow separation.

V. Second Optimization: The Corner Flow Separation Control

A. New Optimization Parameters

The second optimization considers a control with 12 jets (namely, the 10 central jets corresponding to the suboptimum case with $\alpha = 120$ deg and $\beta = 45$ deg) and an additional jet in each corner to control the corner separation. The locations and orientations of the central jets can be seen in Fig. 12d. The new optimization takes into account two others parameters, namely, the streamwise and

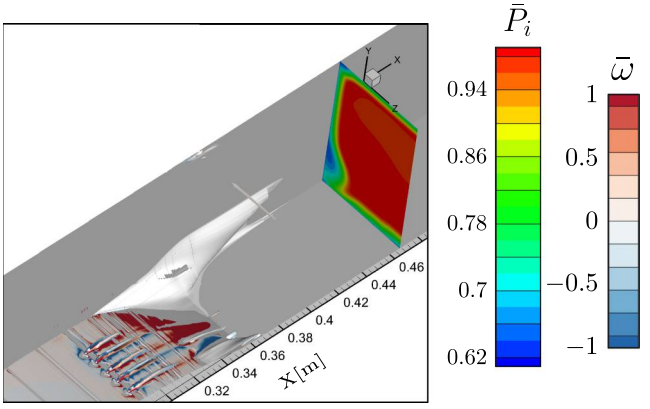

Fig. 16 Nondimensionalized stagnation pressure on DC50 plane, volume of reverse flow (delimited by white surface), and Q criterion equal to $3 \cdot 10^8$ isosurface colorized with longitudinal vorticity for suboptimum case.

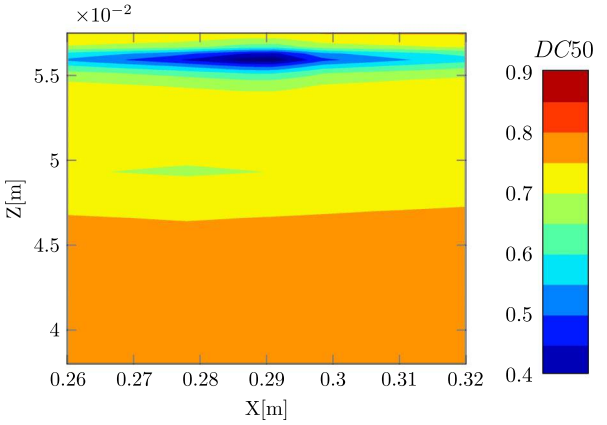

Fig. 17 Zone of interest of the second DC50 model [with $(\alpha, \beta) = (30, 106)$].

lateral positions of the jet. The pitch and skew angles are also to be optimized. The ranges of variation allowed for each parameter are summarized in Table 2.

The objective function is calculated as in the previous optimization.

The problem is of dimension four, and hence the initial number of samples for the Latin hypercube sampling is increased to 15. Then, the process of improvement is kept as before, except that the new points are calculated three by three in order to accelerate the convergence. To choose these three points, the model is updated with the predicted value of the first optimum of the expected improvement, and a new model is computed before a second search of the maximum expected improvement. The same technique is used for the third point. Once the three points have been calculated, their real values are added to the model of the previous step before it is tuned again.

The algorithm enriches the model, reaching a total of 122 points. After a first phase of exploration, the algorithm finds a zone of interest into which it keeps enriching without attempting a new phase of exploration elsewhere in the domain.

B. Results

Overall, DC50 values returned by the model are almost constant and remain close to the one of the suboptimum case of 0.78, meaning that the external jet does not improve the control. Nonetheless, the algorithm manages to find a zone of interest, which is presented on a 2-D map showing the dependence of the DC50 with respect to the longitudinal and lateral locations, with α and β being, respectively, fixed to 30 and 106 deg in Fig. 17a.

In this small zone close to the sidewall, the jet induces an important improvement of the DC50. The longitudinal position is less sensitive than the lateral one, demonstrating that the control efficiency relies on the position of the vortex with respect to the sidewall much more than on its intensity.

The best-controlled case found is for $\alpha = 30$ deg and $\beta = 106$ deg, for which the objective function falls down to 0.34, which represents an improvement of 61% compared to the baseline case. It generates the total pressure distribution presented in Fig. 18a and the reverse flow visible in Fig. 19a.

The corner flow separation is replaced by two smaller separation zones along each side of the corner. These separation zones have

Table 2 Parameter range of the external jet for the second optimization

Parameter	Min	Max
X location, mm	260	320
Z location, mm	38	57.5
Pitch angle α, deg	30	150
Skew angle β, deg	0	180

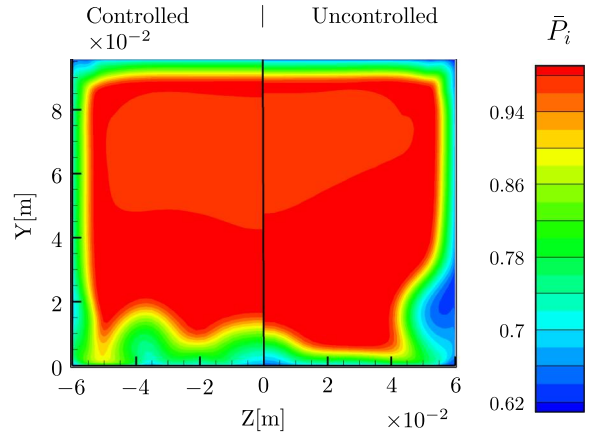

Fig. 18 Nondimensionalized stagnation pressure on transverse DC50 plane of the best-controlled case of the second optimization (left) and uncontrolled case (right).

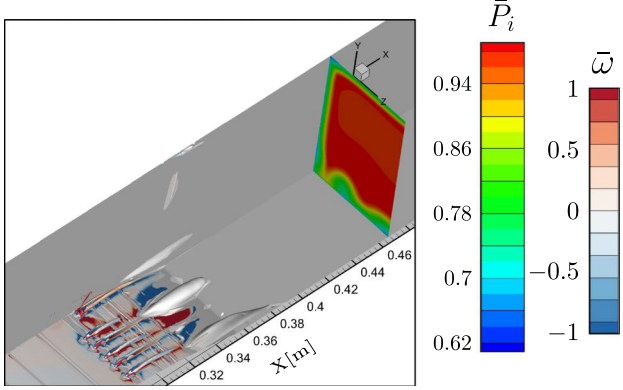

Fig. 19 Nondimensionalized stagnation pressure on DC50 plane, volume of reverse flow (delimited by white surface), and Q criterion equal to $3 \cdot 10^8$ isosurface colorized with longitudinal vorticity for optimum.

smaller impact on the downstream total pressure than the corner flow separation of the reference case. The structure of the corner flow vortex is shown in Fig. 20 in successive transverse planes at $X = 0.295$–0.305–0.315–0.325 and 0.335 m, i.e., from the vortex formation to the beginning of the sidewall separation, which replaces the corner flow separation. The impact of the mixing due to the pair of corotating vortices on the longitudinal momentum field nondimensionalized using $\rho U(X = 0) = 200\ \mathrm{kg \cdot m^{-2} \cdot s^{-1}}$ is visible in Fig. 21, and it can be compared to the uncontrolled case of Fig. 22. In the uncontrolled case, the separation begins between $X = 0.305$

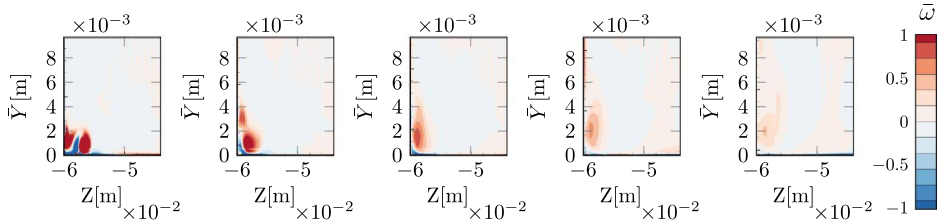

Fig. 20 Nondimensionalized longitudinal vorticity on five transverse planes close to corner, along flow at X equal 0.295, 0.305, 0.315, 0.325, and 0.335 m from left to right for the optimum case of second optimization.

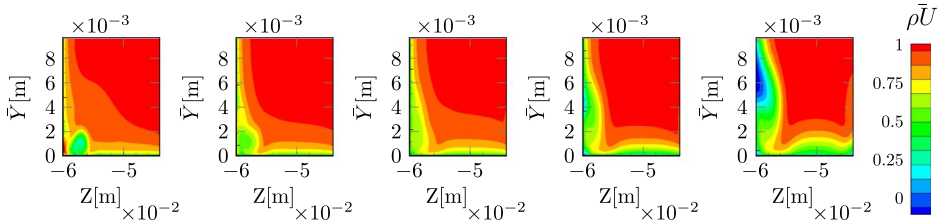

Fig. 21 Nondimensionalized longitudinal momentum on five transverse planes close to corner, along flow at X equal 0.295, 0.305, 0.315, 0.325, and 0.335 m from left to right for optimum case of second optimization.

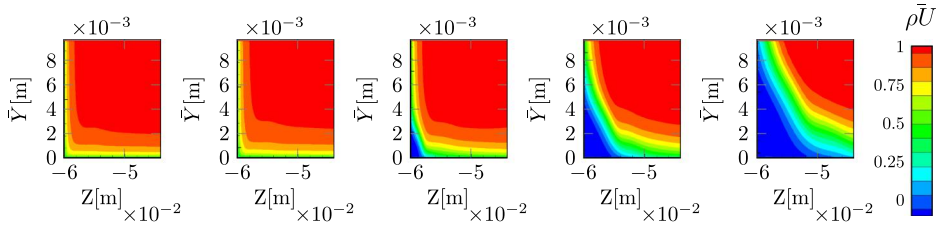

Fig. 22 Nondimensionalized longitudinal momentum on five transverse planes close to corner, along flow at X equal 0.295, 0.305, 0.315, 0.325, and 0.335 m from left to right for uncontrolled case.

and $X = 0.315$ m, and it clearly interacts with both the lower wall and sidewall; whereas in the optimum controlled case, separation occurs between $X = 0.325$ and $X = 0.335$ m and is reduced to a separation on the sidewall. The vortex injects momentum into the boundary layer of the corner flow, and thus prevents its separation. This result is similar to the ones found experimentally in Ref. [50].

Nevertheless, as can be seen in Fig. 18a, compared to Fig. 14b, improvement of the control of the corner flow separation deteriorates the control of the central separation. This confirms the interest of controlling both the boundary layer and the corner flow separation, as was done in Ref. [49].

VI. Further Analysis of the Vorticity Patterns Generated by Downstream- and Upstream-Blowing VGs

To further analyze the fact that the upstream-blowing jets generate a more effective control of the interaction, the data of the cases calculated during the first optimization in Sec. IV are used to devise three models characterizing the physical properties of the vortices produced by a pitched and skewed jet: the norm of the longitudinal vorticity ω, and the coordinates $\bar{Y}_B$ and Z_B of the barycenter of $\|\omega\|$.

Considering one of the jets, ω and the coordinates $\bar{Y}_B$ and Z_B are calculated in a plane located at $X = 0.290$ m. This plane is positioned downstream of the jets at a distance equal to four times the boundary-layer thickness at the jet position: $\delta_j = 2.5$ mm. This distance allows a complete development of the vortical structures while staying in a region where the jet-induced vortices are not yet interacting with the vortices produced by the adjacent jets.

To improve the models by reducing their definition range, besides improving the concentration of the calculated points, the construction of the models takes advantage of the fact that for a single jet considered here, the norm of the longitudinal vorticity and the vertical barycenter are even with both variables considering the point of coordinates (90, 90) as the origin, meaning that for any couple of angles (a, b),

$$\|\omega(a,b)\| = \|\omega(90-(a-90),90-(b-90))\| \tag{4}$$

$$\bar{Y}_B(a,b) = \bar{Y}_B(90-(a-90),90-(b-90)) \tag{5}$$

Furthermore, due to the same symmetry reasons, the lateral position of the barycenter is odd with respect to the same origin, which means

$$Z_B(a,b) = -Z_B(90-(a-90),90-(b-90)) \tag{6}$$

This allows us to construct the models only in the ranges $\alpha = 30$–90 deg and $\beta = 0$–180 deg. The models constructed using the same regression kriging method as in Sec. IV are presented in Fig. 23. Visualization of the vorticity distribution for all the cases presented in Fig. 12 is added on the model of $\|\omega\|$.

The first observation is that there are different configurations of vortices. On the axis $\alpha = 90$ deg, vertical configuration a in Fig. 23 is visible with the strong counter-rotating pair of vortices. This configuration is also visible in Fig. 8 and is close to the flow topology presented in Refs. [18–20].

The second observation is about the axes of $\beta = 0$ deg and $\beta = 180$ deg, where the jet is parallel with the flow. Along these axes, the structure of the vortices is the same as for the vertical case with two counter-rotating vortices with similar shapes and intensities. For the jet blowing downstream (i.e., $\beta = 0$ deg), when α decreases, $\|\omega\|$ decreases too, and the barycenter is moving from slightly above the boundary layer to one-quarter below it. On the contrary, for the upstream-blowing jet (i.e., $\beta = 180$ deg), when α decreases, the barycenter moves away from the boundary layer up to $1.1\delta_j$ with $\|\omega\|$ also decreasing. This is consistent with the fact that the upstream-blowing jet is turned downward during the mixing of the jet. It is important to notice that the vortices produced by this type of interaction (case c) are more spread out than in the

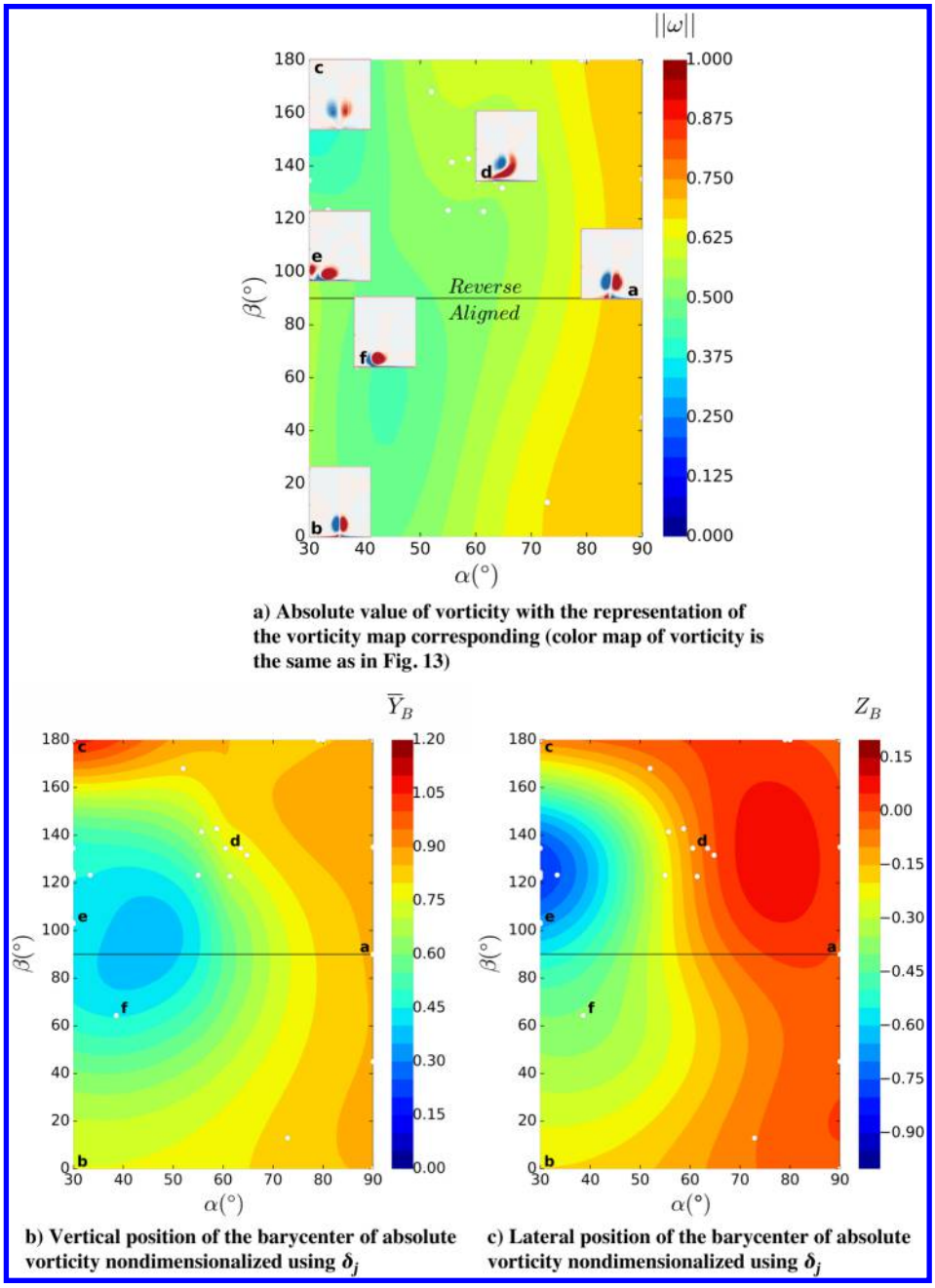

a) Absolute value of vorticity with the representation of the vorticity map corresponding (color map of vorticity is the same as in Fig. 13)

b) Vertical position of the barycenter of absolute vorticity nondimensionalized using δ_j

c) Lateral position of the barycenter of absolute vorticity nondimensionalized using δ_j

Fig. 23 Models of functions calculated on a plane at $X = 0.290$ m for one VG; letters correspond to cases presented in Fig. 12.

downstream-blowing case. This known behavior is used to enhance mixing in the scramjet combustion chamber [51].

Considering an axis for $\beta = 90$ deg, we confirm a result found in Ref. [25] and others, namely, the decrease of the total amount of streamwise vorticity with a decrease of the pitch angle. As noticed in Ref. [52], this structure transitioned from a pair of counter-rotating vortices to a strongly unbalanced pair of vortices, as is visible in case f. The weaker vortex vanishes more rapidly in the flow and, further downstream, the vorticity pattern reduces to a strong unique vortex.

In Fig. 23b, the vortices tend to be located at the edge of the boundary layer, which intensifies the mixing between the boundary layer and the contiguous flow.

Another interesting point is that the vortical structure developed by an upstream-blowing jet does not undergo the same topology change as for the downstream-blowing jet. There is a transition from case f to case d, which passes by case e. This specific case generates lower vorticity but, as it forms a pair of same-sign vortices, this generates a large lateral displacement, as can be seen in Fig. 23c. This allows the structure to have a smoother mixing on a wider extent.

Using these models, the mechanism leading to the optimum control of the first optimization can be explained as follows: this couple of angles $[(\alpha, \beta) = (30, 102.8)]$ generates for each jet a pair of same-sign streamwise vortices, as can be seen in Fig. 24a. This pair of vortices generates a lateral velocity. Considering in Fig. 24b the development of the vortices farther downstream, in the case of the central jets, the two vortices merge when they meet the adjacent opposite vortices to form a new pair of opposite vortices that sustain each other in the downstream flow direction. Considering the outer jet, the pair of vortices moves closer to the wall and produces a mixing that induces a region where the boundary layer presents a deficit of streamwise momentum between the two vortices. This weaker zone is more sensitive to the adverse pressure gradient due to the shock and

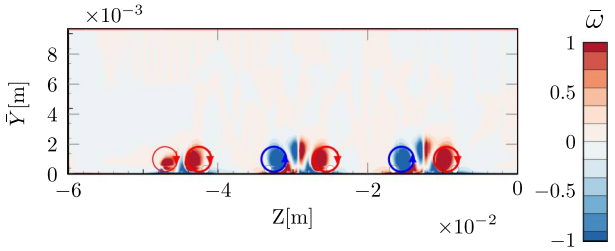

a) Longitudinal vorticity at X = 0.290 m: optimum case of the first optimization

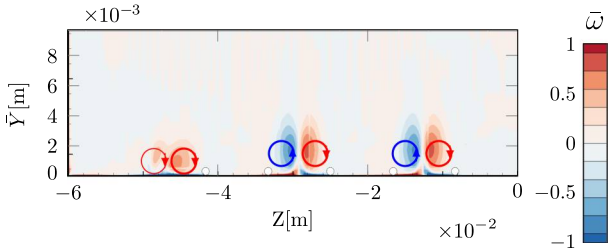

b) Longitudinal vorticity at X = 0.310 m: optimum case of the first optimization

Fig. 24 Nondimensionalized longitudinal vorticity on two transverse planes along the flow; white dots represent lateral positions of the jets.

separates earlier than the corner flow. This modifies the corner flow separation, with this new structure having a less significant impact on the stagnation pressure farther downstream.

VII. Conclusions

The optimization process based on RANS computations and a kriging metamodel is an effective method to identify the optimal pitch and skew angles of 10 fluidic VGs used to control a transonic shock-wave/boundary-layer interaction. This fluidic control configuration with jet pitch angles equal to 30 deg and skew angles equal to ±102.8 deg (i.e., upstream-blowing jets) has not been studied to the authors' knowledge. This configuration makes the objective function, which is the DC50 criterion, fall down by 22%.

To improve this first result, a second optimization has been implemented, which focuses on the control of the corner flow separation by adding two lateral jets to a suboptimal configuration of the first optimization. These added VGs were optimized in pitch angle, skew angle, and lateral and longitudinal positions. The algorithm detects a zone of interest in which the DC50 criterion is reduced by 61%. This configuration only requires a momentum coefficient c_μ of 0.03%, which makes it an efficient control. The jets added in the optimal configuration blows slightly upstream with a pitch angle of 30 deg and a skew angle of 106 deg. This optimum control of the corner flow separation is possible in a narrow lateral zone close to the sidewall, with the choice of longitudinal position being much less determinant in terms of control performance.

This study highlights the interest of a global approach for the design of a SWBLI control because of the existence of a massive central separation strongly influenced by corner flow separation. These central and corner flow separations are linked to the intensity and shape of the shock wave, which make such an interaction a complex multiparameter 3-D phenomenon.

The present study demonstrates that upstream-blowing jets can be efficient to control a flow destabilized by a strong SWBLI. Compared to jets blowing downstream, upstream-blowing jets generate vorticity structures having different vertical and lateral velocities. Their capacity to generate a pair of corotating vortices close to the wall allows for a larger lateral displacement of the vortices, which induces a wider mixing of the boundary layer.

Following this numerical study, the best controlled configuration will be tested in a wind tunnel in order to deeply understand the mechanism of control and to characterize its unsteady features.

Acknowledgments

This work was supported by the Direction Générale de l'Armement. Their support is gratefully acknowledged. The authors are especially grateful to J. Délery for helpful discussions and advice during the synthesis of the study.

References

[1] Delery, J. M., "Shock Wave/Turbulent Boundary Layer Interaction and Its Control," *Progress in Aerospace Sciences*, Vol. 22, No. 4, 1985, pp. 209–280. https://doi.org/10.1016/0376-0421(85)90001-6

[2] Babinsky, H., and Harvey, J. K., *Shock Wave-Boundary-Layer Interactions*, Cambridge Univ. Press, Cambridge, England, U.K., 2011.

[3] Dolling, D. S., "Fifty Years of Shock-Wave/Boundary-Layer Interaction Research: What Next?" *AIAA Journal*, Vol. 39, No. 8, 2001, pp. 1517–1531. https://doi.org/10.2514/2.1476

[4] Gaitonde, D. V., "Progress in Shock Wave/Boundary Layer Interactions," *Progress in Aerospace Sciences*, Vol. 72, Jan. 2015, pp. 80–99. https://doi.org/10.1016/j.paerosci.2014.09.002

[5] Lin, J., Howard, F., Bushnell, D., and Selby, G., "Investigation of Several Passive and Active Methods for Turbulent Flow Separation Control," *21st Fluid Dynamics, Plasma Dynamics and Lasers Conference*, AIAA Paper 1990-1598, 1990. https://doi.org/10.2514/6.1990-1598

[6] Babinsky, H., and Ogawa, H., "SBLI Control for Wings and Inlets," *Shock Waves*, Vol. 18, No. 2, 2008, pp. 89–96. https://doi.org/10.1007/s00193-008-0149-7

[7] Rosenblum, J.-P., "An Overview of Flow Control Activities at Dassault Aviation over the Last 25 Years," *Aeronautical Journal*, Vol. 120, No. 1225, 2016, pp. 391–414. https://doi.org/10.1017/aer.2016.9

[8] Ternoy, F., Dandois, J., David, F., and Pruvost, M., "Overview of Onera Actuators for Active Flow Control," *Journal of AerospaceLab*, Vol. 6, June 2013, pp. 1–14, https://hal.archives-ouvertes.fr/hal-01184470.

[9] Benard, N., and Moreau, E., "Electrical and Mechanical Characteristics of Surface AC Dielectric Barrier Discharge Plasma Actuators Applied to Airflow Control," *Experiments in Fluids*, Vol. 55, No. 11, 2014, Paper 1846. https://doi.org/10.1007/s00348-014-1846-x

[10] Chiatto, M., and de Luca, L., "Numerical and Experimental Frequency Response of Plasma Synthetic Jet Actuators," *55th AIAA Aerospace Sciences Meeting*, AIAA Paper 2017-1884, 2017. https://doi.org/10.2514/6.2017-1884

[11] Staudenmeyer, J., Schnoebel, N., and Rist, U., "Wall Temperature and Suction Control of Linear Modes in Compressible Corner Flow," *AIAA Journal*, Vol. 57, No. 6, 2019, pp. 2335–2343. https://doi.org/10.2514/1.J057993

[12] Sharma, S., Shadloo, M. S., Hadjadj, A., and Kloker, M. J., "Control of Oblique-Type Breakdown in a Supersonic Boundary Layer Employing Streaks," *Journal of Fluid Mechanics*, Vol. 873, 2019, pp. 1072–1089. https://doi.org/10.1017/jfm.2019.435

[13] Crowther, W., Jabbal, M., and Liddle, S., "Flow Control Fallacies: A Review of Commonpitfalls in Flow Control Research," *Journal of Aerospace Engineering*, Vol. 225, No. 1, 2011, pp. 1–11. https://doi.org/10.1243/09544100 JAERO761

[14] Lin, J. C., "Review of Research on Low-Profile Vortex Generators to Control Boundary-Layer Separation," *Progress in Aerospace Sciences*, Vol. 38, Nos. 4–5, 2002, pp. 389–420. https://doi.org/10.1016/S0376-0421(02)00010-6

[15] Lee, S., Loth, E., and Babinsky, H., "Normal Shock Boundary Layer Control with Various Vortex Generator Geometries," *Computers and Fluids*, Vol. 49, No. 1, 2011, pp. 233–246. https://doi.org/10.1016/j.compfluid.2011.06.003

[16] Titchener, N., and Babinsky, H., "A Review of the Use of Vortex Generators for Mitigating Shock-Induced Separation," *Shock Waves*, Vol. 25, No. 5, 2015, pp. 473–494. https://doi.org/10.1007/s00193-015-0551-x

[17] Bur, R., Coponet, D., and Carpels, Y., "Separation Control by Vortex Generator Devices in a Transonic Channel Flow," *Shock Waves*, Vol. 19, No. 6, 2009, pp. 521–530. https://doi.org/10.1007/s00193-009-0234-6

[18] Margason, R. J., *Fifty Years of Jet in Cross Flow Research*, AGARD CP-534, Neuilly-Sur-Seine, France, 1993, pp. 1–2.

[19] Jacquin, L., "Phenomenological Description and Simplified Modeling of the Vortex Wake Issuing from a Jet in a Cross-Flow," *Aerospace Research*, No. 2, 1994, pp. 117–133.

[20] Karagozian, A. R., "The Jet in Crossflow," *Physics of Fluids*, Vol. 26, No. 10, 2014, Paper 101303.
https://doi.org/10.1063/1.4895900

[21] Ilak, M., Schlatter, P., Bagheri, S., and Henningson, D. S., "Bifurcation and Stability Analysis of a Jet in Cross-Flow: Onset of Global Instability at a Low Velocity Ratio," *Journal of Fluid Mechanics*, Vol. 696, 2012, pp. 94–121.
https://doi.org/10.1017/jfm.2012.10

[22] Pearcey, H., Rao, K., and Sykes, D., "Inclined Air-Jets Used as Vortex Generators to Suppress Shock-Induced Separation," *Computational and Experimental Assessment of Jets in Cross Flow*, AGARD CP-534, Neuilly-Sur-Seine, France, Nov. 1993, pp. 40.1–40.10.

[23] Godard, G., and Stanislas, M., "Control of a Decelerating Boundary Layer. Part 3: Optimization of Round Jets Vortex Generators," *Aerospace Science and Technology*, Vol. 10, No. 6, 2006, pp. 455–464.
https://doi.org/10.1016/j.ast.2005.11.005

[24] Verma, S. B., Manisankar, C., and Akshara, P., "Control of Shock-Wave Boundary Layer Interaction Using Steady Micro-Jets," *Shock Waves*, Vol. 25, No. 5, 2015, pp. 535–543.
https://doi.org/10.1007/s00193-014-0508-5

[25] Beresh, S. J., Henfling, J. F., Erven, R. J., and Spillers, R. W., "Vortex Structure Produced by a Laterally Inclined Supersonic Jet in Transonic Crossflow," *Journal of Propulsion and Power*, Vol. 23, No. 2, 2007, pp. 353–363.
https://doi.org/10.2514/1.25444

[26] Souverein, L. J., and Debiève, J.-F., "Effect of Air Jet Vortex Generators on a Shock Wave Boundary Layer Interaction," *Experiments in Fluids*, Vol. 49, No. 5, 2010, pp. 1053–1064.
https://doi.org/10.1007/s00348-010-0854-8

[27] Sartor, F., "Unsteadiness in Transonic Shock-Wave/Boundary-Layer Interactions: Experimental Investigation and Global Stability Analysis," Ph.D. Thesis, Aix-Marseille Univ., Marseille, France, March 2014.

[28] Sartor, F., Losfeld, G., and Bur, R., "PIV Study on a Shock-Induced Separation in a Transonic Flow," *Experiments in Fluids*, Vol. 53, No. 3, 2012, pp. 815–827.
https://doi.org/10.1007/s00348-012-1330-4

[29] Sartor, F., Mettot, C., Bur, R., and Sipp, D., "Unsteadiness in Transonic Shock-Wave/Boundary-Layer Interactions: Experimental Investigation and Global Stability Analysis," *Journal of Fluid Mechanics*, Vol. 781, Oct. 2015, pp. 550–577.
https://doi.org/10.1017/jfm.2015.510

[30] Benoit, C., Péron, S., and Landier, S., "Cassiopee: A CFD Pre- and Post-Processing Tool," *Aerospace Science and Technology*, Vol. 45, Sept. 2015, pp. 272–283.
https://doi.org/10.1016/j.ast.2015.05.023

[31] Hue, D., Chanzy, Q., and Landier, S., "DPW-6: Drag Analyses and Increments Using Different Geometries of the Common Research Model Airliner," *Journal of Aircraft*, Vol. 55, No. 4, 2018, pp. 1509–1521.
https://doi.org/10.2514/1.C034139

[32] Cambier, L., Heib, S., and Plot, S., "The Onera elsA CFD Software: Input from Research and Feedback from Industry," *Mechanics and Industry*, Vol. 14, No. 3, 2013, pp. 159–174.
https://doi.org/10.1051/meca/2013056

[33] Dandois, J., "Improvement of Corner Flow Prediction Using the Quadratic Constitutive Relation," *AIAA Journal*, Vol. 52, No. 12, 2014, pp. 2795–2806.
https://doi.org/10.2514/1.J052976

[34] Cartieri, A., Hue, D., Chanzy, Q., and Atinault, O., "Experimental Investigations on the Common Research Model at ONERA-S1MA–Comparison with DPW Numerical Results," *Journal of Aircraft*, Vol. 55, No. 4, 2018, pp. 1491–1508.
https://doi.org/10.2514/1.C034414

[35] Evans, A. J., Caulfield, C. P., and Woods, A. W., "Linear Estimation of Flux Sensitivity to Uncertainty in Porous Media," *Journal of Fluid Mechanics*, Vol. 768, 2015, pp. 600–622.
https://doi.org/10.1017/jfm.2015.102

[36] Toal, D. J., Bressloff, N. W., and Keane, A. J., "Kriging Hyperparameter Tuning Strategies," *AIAA Journal*, Vol. 46, No. 5, 2008, pp. 1240–1252.
https://doi.org/10.2514/1.34822

[37] Chanzy, Q., and Keane, A. J., "Analysis and Experimental Validation of Morphing UAV Wings," *Aeronautical Journal*, Vol. 122, No. 1249, 2018, pp. 390–408.
https://doi.org/10.1017/aer.2017.130

[38] Forrester, A., Sobester, A., and Keane, A., *Engineering Design via Surrogate Modelling: A Practical Guide*, Wiley, Hoboken, NJ, 2008.

[39] Morris, M. D., and Mitchell, T. J., "Exploratory Designs for Computational Experiments," *Journal of Statistical Planning and Inference*, Vol. 43, No. 3, 1995, pp. 381–402.
https://doi.org/10.1016/0378-3758(94)00035-T

[40] Forrester, A. I., and Keane, A. J., "Recent Advances in Surrogate-Based Optimization," *Progress in Aerospace Sciences*, Vol. 45, No. 1, 2009, pp. 50–79.
https://doi.org/10.1016/j.paerosci.2008.11.001

[41] Jones, D. R., "A Taxonomy of Global Optimization Methods Based on Response Surfaces," *Journal of Global Optimization*, Vol. 21, No. 4, 2001, pp. 345–383.
https://doi.org/10.1023/A:1012771025575

[42] Amitay, M., Smith, D. R., Kibens, V., Parekh, D. E., and Glezer, A., "Aerodynamic Flow Control over an Unconventional Airfoil Using Synthetic Jet Actuators," *AIAA Journal*, Vol. 39, No. 3, 2001, pp. 361–370.
https://doi.org/10.2514/2.1323

[43] Godard, G., and Stanislas, M., "Control of a Decelerating Boundary Layer. Part 1: Optimization of Passive Vortex Generators," *Aerospace Science and Technology*, Vol. 10, No. 3, 2006, pp. 181–191.
https://doi.org/10.1016/j.ast.2005.11.007

[44] Goldsmith, E. L., and Seddon, J., *Practical Intake Aerodynamic Design*, AIAA, Washington, D.C., 1993.

[45] Garnier, E., "Flow Control by Pulsed Jet in a Curved S-Duct: A Spectral Analysis," *AIAA Journal*, Vol. 53, No. 10, 2015, pp. 2813–2827.
https://doi.org/10.2514/1.J053422

[46] Rao, M., "An Experimental Investigation of the Use of Air Jet Vortex Generators to Control Shock Induced Boundary Layer Separation," Ph.D. Thesis, City, Univ. of London, London, 1988.

[47] Bray, T. P., and Garry, K. P., "Optimisation of Air-Jet Vortex Generators with Respect to System Design Parameters," *Aeronautical Journal*, Vol. 103, No. 1028, 1999, pp. 475–480.
https://doi.org/10.1017/S0001924000064423

[48] Dandois, J., Brunet, V., Molton, P., Abart, J.-C., and Lepage, A., "Buffet Control by Means of Mechanical and Fluidic Vortex Generators," *5th Flow Control Conference*, AIAA Paper 2010-4975, 2010.
https://doi.org/10.2514/6.2010-4975

[49] Titchener, N., and Babinsky, H., "Shock Wave/Boundary-Layer Interaction Control Using a Combination of Vortex Generators and Bleed," *AIAA Journal*, Vol. 51, No. 5, 2013, pp. 1221–1233.
https://doi.org/10.2514/1.J052079

[50] Xiang, X., and Babinsky, H., "An Experimental Study of Corner Flow Control Applied to an Oblique Shock-Wave/Boundary-Layer Interaction," *2018 AIAA Aerospace Sciences Meeting*, AIAA Paper 2018-1532, 2018.
https://doi.org/10.2514/6.2018-1532

[51] Han, D., Orozco, V., and Mungal, M., "Gross-Entrainment Behavior of Turbulent Jets Injected Obliquely into a Uniform Crossflow," *AIAA Journal*, Vol. 38, No. 9, 2000, pp. 1643–1649.
https://doi.org/10.2514/2.1147

[52] Feng, Y.-Y., Song, Y.-P., and Breidenthal, R. E., "Model of the Trajectory of an Inclined Jet in Incompressible Crossflow," *AIAA Journal*, Vol. 56, No. 2, 2018, pp. 458–464.
https://doi.org/10.2514/1.J056181

F. Grasso
Associate Editor